

ESTIMATION OF FLUID FLOW FIELDS AND THEIR STAGNATION POINTS

Rasmus Larsen

TECHNICAL REPORT

IMM-REP-97-17

IMM

ESTIMATION OF FLUID FLOW FIELDS AND THEIR STAGNATION POINTS

Rasmus Larsen

TECHNICAL REPORT

IMM-REP-97-17

IMM

and The Flow Stagnation Points
Rasmus Larsen
Department of Mathematical Modelling
Technical University of Denmark, Building 321, DK-2800 Lyngby

E-mail: rl@imm.dtu.dk
URL: <http://www.imm.dtu.dk>
Phone: +45 4588 1433
FAX: +45 4588 1397

Keywords

Optical flow, stagnation points, linear phase model, ventilation.

Abstract

Given a temporal sequence of images of fluids we will use local polynomials to regularise observations of normal flows into smooth flow fields. This technique furthermore allows us to give a qualitative local description of the flow field and to estimate the position of stagnation points. The algorithm is applied to two data sets. First a series of Meteosat images are processed with the purpose of estimating cloud motion. Secondly, the airflow in livestock buildings is estimated using the technique on images recorded of smoke patterns illuminated by a laser sheet. Here the purpose is the evaluation of the ventilation system.

I Introduction

The estimation of flow fields is usually implemented as a two-step procedure. First, local estimates of (normal) flow are extracted from the image sequence based on an assumption of conservation of some image feature over time. This image feature may be the intensity of a pixel itself, or it may be some function (e.g. the Laplacian) of the image intensities. The techniques for the local estimation of flow usually also assume that locally the image features move with constant velocity. The techniques for estimating the local flow field include correlation methods (Leese & Novak, 1971; Anandan, 1989; Schmetz & Holmlund, 1993), differential methods (Horn & Schunk, 1981; Nagel & Enkelmann, 1986), energy-based methods (Adelson & Bergen, 1985; Heeger, 1987; Knutsson, 1989) and phase-based methods (Fleet & Jepson, 1990). Some of these techniques even include the possibility of quantifying the directional certainty with which the flow has been estimated locally. In (Anandan, 1989) the curvature of the match surface is used, Nagel & Enkelmann (1986) use second order spatial derivatives to identify the neighbourhood under investigation. In the second

by using sets of orthogonal basis functions. This can be done by applying a regularisation that forces the spatial derivatives to be small. Such methods include (Horn & Schunk, 1981; Nagel & Enkelmann, 1986; Terzopoulos, 1986; Konrad & Dubois, 1992). Other approaches are based on spatial filtering (e.g. (Simpson & Gobat, 1994)).

As the first step we will apply an energy-based method described in (Larsen, Conradsen, & Ersbøll, 1995) that allows for the extraction of velocity estimates as well as related directional probabilities of the estimates based on the local energy distribution. This technique is described in Section II-A.

In Section II-B we will describe a technique for integrating the locally estimated (normal) flows that is based on approximating a first order polynomial to each of the velocity components in a neighbourhood of every pixel. In addition to providing a regularised flow field the polynomial parameters also allow for the classification of the flow into a number of descriptors corresponding to the Jordan canonical forms of the matrix that describe the flow. A similar technique is used by Rao & Jain (1992) for the purpose of classifying oriented texture fields. Herlin, Cohen, & Bouzidi (1995) use this type of method for the detection and tracking of vortices from a series of flow fields corresponding to the temporal evolution of ocean temperature patterns. However, in this work the flow fields are first extracted using an elaborated version of the regularisation technique originally described by Horn & Schunk (1981), after which the different high-order structures are identified. In this work we propose a technique that allows for simultaneous estimation of high-order structures (such as vortices) and regularised flow fields.

In Section IV we will show how the proposed technique may be used to estimate fluid flow fields in two cases. First we consider a temporal sequence of meteorological images from the Meteosat satellite, and secondly, we will use the method in order to estimate the air flow in livestock buildings. In both cases the topological features (i.e. stagnations points) are extracted.

II Methods

A Local Velocity Estimation

Consider a neighbourhood containing a one dimensional intensity structure (e.g., a line) that translates coherently through time. In the spatio-temporal domain this corresponds to a neighbourhood of iso-grey level planes. Let these planes be given by their unit normal vector $\mathbf{k} = (k_1, k_2, k_3)^T$. We will refer to this vector as the spatio-temporal orientation vector. The non-zero Fourier coefficients of this neighbourhood are concentrated to the line defined by \mathbf{k} .

The relationship between the spatio-temporal orientation vector and the normal flow vector $\boldsymbol{\mu} = (\mu, \nu)^T$ is illustrated in Fig. 1. In this figure a line translating with constant velocity through space is shown at four time instances. These lines span a plane in space-time, \mathbf{k} is the normal vector of this plane. In the figure $\boldsymbol{\mu}^* = (\mu, \nu, 1)^T$ and the line orientation vector $\mathbf{e} = (-k_2, k_1, 0)^T$. Because $\boldsymbol{\mu}^*$ is perpendicular to \mathbf{k} as well as \mathbf{e} , its direction is given by the outer product of these vectors. Finally this outer product should be normed so that the temporal coordinate equals 1. This results

$$\boldsymbol{\mu} = (\mu, \nu)^T = \frac{-k_3}{k_1^2 + k_2^2} (k_1, k_2)^T \quad (1)$$

Now, in order to estimate the spatio-temporal orientation vector, we will sample the Fourier domain using a set of spatio-temporal filters. Using a method developed by Knutsson (1989) this can be achieved by applying a set of directional quadrature filter pairs symmetrically distributed over the spatio-temporal orientation space. As an approximation to such a set of filters we will employ a set of 6 Gabor filters (Gabor, 1946) with center frequencies given by the vertices of a semi-icosahedron. Finally, the energy distribution of the Fourier domain as estimated by the set of quadrature filter pairs may be represented by the tensor (e.g. (Knutsson, 1989))

$$\mathbf{T} = \sum_{p=1}^6 q_p \mathbf{n}_p \mathbf{n}_p^T \quad (2)$$

where q_p is the output from the p th quadrature filter pair, and \mathbf{n}_p is the unit normal vector defining the direction of the filter.

In order to find the direction of maximum spectral density we must find the unit vector \mathbf{k} that maximises $\mathbf{k}^T \mathbf{T} \mathbf{k}$. This vector is the eigenvector corresponding to the largest eigenvalue of \mathbf{T} (e.g. (Anderson, 1984)). So for the coherently translating one-dimensional intensity structure, which has an effectively one dimensional Fourier domain, the spatio-temporal orientation vector is found by an eigen analysis of \mathbf{T} . Because the Fourier domain is one dimensional, \mathbf{T} has only one non-zero eigenvalue.

Now, if the translating structure has a two-dimensional intensity structure (e.g., a grey level corner) the spatio-temporal domain is described by two spatio-temporal orientations, each of which give rise to a non-zero eigenvalue of \mathbf{T} . The eigenvectors corresponding to these non-zero eigenvalues each corresponds to a normal flow by using Equation (1).

Given the true flow we may determine the difference between the projection of the true flow on to either of these estimated normal flows and the normal flows themselves

$$d_k(\mathbf{x}_i) = |(\mathbf{u}(\mathbf{x}_i) - \boldsymbol{\mu}_k(\mathbf{x}_i))^T \cdot \frac{\boldsymbol{\mu}_k(\mathbf{x}_i)}{\|\boldsymbol{\mu}_k(\mathbf{x}_i)\|}|, \quad k = 1, 2 \quad (3)$$

where $\mathbf{u}(\mathbf{x}_i)$, $\boldsymbol{\mu}_k(\mathbf{x}_i)$ are the true flow and the estimated normal flows taken at the position \mathbf{x}_i . It is the (weighted) sum of squares of these distances that should be minimised in order to obtain an estimate of the velocity field.

Deviation from the assumption of coherent translation, imperfectly designed filters and noise will result in non-zero Fourier coefficients not being contained in one single line or plane. In this case all three of the tensor eigenvalues will be non-zero. This allows us to extract information about the quality of the estimates of normal flows we get from the eigenvectors corresponding to the two largest eigenvalues. Because imperfect conditions result in a non-zero third eigenvalue we suggest using a confidence measure for each of the linear constraints based on the difference of the corresponding eigenvalue and the least eigenvalue. Furthermore, a normalisation of this difference should be made. This is evident as a noise free high step edge measures the motion just as well as

$$w_k(\mathbf{x}_i) = \frac{\kappa(\mathbf{x}_i) - \kappa(\mathbf{x}_i)}{\kappa(\mathbf{x}_i)}, \quad k = 1, 2 \quad (4)$$

Where $\kappa(\mathbf{x}_i) \geq \kappa(\mathbf{x}_i) \geq \kappa(\mathbf{x}_i) \geq 0$ denote the eigenvalues of the tensor at position \mathbf{x}_i . This confidence measure approaches zero when the difference of the corresponding eigenvalue and the least eigenvalue approaches zero, and it attains its maximum value of one, when the least eigenvalue is zero, and the corresponding eigenvalue is the largest, or is equal to the largest eigenvalue, respectively.

B Integration of Local Measurements

As mentioned in the Introduction we will approximate our flow field by local first order polynomials in the spatial coordinates, i.e. in the vicinity of the position $\mathbf{x}_i = (x_i, y_i)^T$ the flow field may be parametrised like this

$$\mathbf{u}(\mathbf{x}) = \mathbf{A}_i(\mathbf{x} - \mathbf{x}_i) + \mathbf{b}_i, \quad \mathbf{x} \in N_i, \quad (5)$$

where N_i denote the set of pixels in the neighbourhood of pixel i . We will estimate the parameters of this model for every pixel by minimising the sum of the squared differences within a neighbourhood between the model and the observations of normal flows given by Equation (3), i.e.

$$\begin{aligned} (\hat{\mathbf{A}}_i, \hat{\mathbf{b}}_i) = & \quad (6) \\ \arg \min_{\mathbf{A}_i, \mathbf{b}_i} \text{OBJ}(\mathbf{A}_i, \mathbf{b}_i) = & \\ \arg \min_{\mathbf{A}_i, \mathbf{b}_i} \sum_{j \in N_i} \sum_{k=1}^2 w_k(\mathbf{x}_j) \left[((\mathbf{A}_i(\mathbf{x}_j - \mathbf{x}_i) + \mathbf{b}_i) - \boldsymbol{\mu}_k(\mathbf{x}_j))^T \cdot \frac{\boldsymbol{\mu}_k(\mathbf{x}_j)}{\|\boldsymbol{\mu}_k(\mathbf{x}_j)\|} \right]^2 & \end{aligned}$$

By differentiating with respect to the parameters and setting the partial derivatives equal to zero we find that the estimate of the flow field is obtained by solving a six dimensional linear system for every pixel in our image.

It is evident from Equation (5) that the estimate of the flow field at pixel i is given by

$$\hat{\mathbf{u}}(\mathbf{x}_i) = \hat{\mathbf{b}}_i. \quad (7)$$

Furthermore, we may characterise the type of the flow field in the vicinity of \mathbf{x}_i depending on the nature of the matrix \mathbf{A}_i . Following Rao & Jain (1992), if \mathbf{A}_i is non-singular, the local model of the flow field has exactly one stagnation point (i.e. a point \mathbf{c} satisfying $\mathbf{u}(\mathbf{c}) = \mathbf{0}$), and this point is given by

$$\mathbf{c}_i = \mathbf{x}_i - \hat{\mathbf{A}}_i^{-1} \hat{\mathbf{b}}_i. \quad (8)$$

Moreover, based on the eigenvalues, λ_1 and λ_2 of \mathbf{A}_i we may classify the type of neighbourhoods into a finite number of classes (Rao & Jain, 1992; Herlin et al., 1995)

1. λ_1 and λ_2 are real, and $\lambda_1, \lambda_2 > 0$: \mathbf{c}_i is a node

3. λ_1 and λ_2 are complex: c_i is a center or a spiral.

If, on the other hand, A_i is singular, it has either rank 1 or 0. In the first case, there is a line of stagnation points, in the second case, the flow field is constant.

III Data

A Case 1: Cloud flow fields.

The image sequence used here was recorded by the Meteosat 5 satellite. The images are from the infrared channel (10.5 - 12.5 μm). Preliminary processing performed by the Danish Meteorological Institute consist of mapping to a polar stereographic projection, interpolation to a equirectangular 7 km grid, and subsection to 384×512 images. The center of the grid is at 48.4° N latitude and 8.2° E longitude. The images are recorded with a time interval of 30 minutes. Furthermore, the image sequence has been down sampled by a factor 4.

B Case 2: Livestock Building Airflow.

The data have been recorded at the Department of Agricultural Engineering and Production Systems at the Danish Institute of Animal Science using a light sensitive consumer video camera (frame rate: 25 Hz). All measurements are carried out under iso-thermic conditions. The experimental setup is shown in Figure 2. The Plexiglass model of the segment of a pigs sty is 1 m broad and 0.5 m deep. The air velocity in the inlet is measured to 3 m/s. Smoke is induced in the airflow at the inlet. The laser illuminated plane is placed in the center of the model

IV Results

For both sequence we have used a set of Gabor filters with the bandwidth in octaves measured at one standard deviation of the Gaussian envelope set to 1, and the standard deviation of the Gaussian envelope set to 2 pixels. The Gaussian envelope was truncated at ± 2.5 standard deviations. Using Equation (1) we obtain the estimates of normal flow. These are then integrated by fitting the first order polynomial model to the flow locally. For this procedure a circular window with a radius of 20 pixels has been used. In Figures 4 and 7 the estimated flow field for the cases are shown.

Finally, again following Rao & Jain (1992), we may estimate the stagnation points of the global flow field. Because parts of a given pattern (e.g. a spiral) is observed in several neighbourhoods, we may gather "votes" for the candidates for the stagnation point from each of these neighbourhoods. Suppose we find estimates \hat{A}_i and \hat{b}_i in a given neighbourhood N_i . From these estimates we

having a stagnation point at $c_i = -A_i^{-1} b_i$. We may then increment a measure for the likelihood of a stagnation point of type P_l being at c_i . Consequently, two neighbourhoods in two different sections of the same (spiral) pattern will update the likelihood measure at the same stagnation point. In our case we have three of these likelihood measures (which in a sense corresponds to Hough-like accumulator arrays), one for each of the patterns (e.g. node, saddle, center/spiral) listed in Section II-B. We will increment the likelihood measure by the inverse of the value of the object function OBJ in Equation (6). The reason for this is that the "vote" for a particular stagnation point should be weighted by the closeness of fit of the model at the neighbourhood that casts this vote.

In Figures 5 and 8 thresholded versions of these likelihood measures are shown for both cases. In Figure 5 we see two clusters of points corresponding to the two centers that are easily identified in the flow field in Figure 4. In the livestock building case, in Figure 8, the single center seen in Figure 7 is also identified.

V Conclusion

This paper has presented a method to integrate estimates of normal flows into smooth flow fields using a local first order polynomial model for the flow vectors. This model furthermore allows for an interpretation of the type of pattern (i.e. vortex, spiral, node, saddle) that the area under consideration is part of, and enables us to estimate the position of the stagnation (i.e. fixed) point for that particular pattern. The position and type of stagnation points gives a topological description of the flow field.

Furthermore, results on applying this technique have been demonstrated for two cases. The first case is a sequence of infrared images from the European meteorological satellite Meteosat, the second sequence visualises the airflow in livestock buildings by means of inserting smoke in the air inlets and recording the moving smoke patterns that are illuminated by a laser sheet. In both cases the global flow field has been successfully estimated and stagnation points found and identified.

VI Acknowledgements

The author wish to thank Senior Scientist Hans H. Valeur and Poul Nielsen, the Danish Meteorological Institute, for providing the Meteosat data.

Senior scientists Svend Morsing and Jan Strøm from the Department of Agricultural Engineering and Production Systems at the Danish Institute of Animal Science designed the experimental setup for the livestock model experiment. The data collection was carried out by Technician Peter Ravn. Their work is hereby gratefully acknowledged.

Finally, the financial support for this work of The Danish Agricultural and Veterinary Research Council is gratefully acknowledged.

- Adelson, E. H. & Bergen, J. R. (1985). Spatiotemporal energy models for the perception of motion. *Journal of the Optical Society of America, Series A*, **2**(2), 284–299.
- Anandan, P. (1989). A computational framework and an algorithm for the measurement of visual motion. *International Journal of Computer Vision*, **2**, 283–310.
- Anderson, T. W. (1984). *An Introduction to Multivariate Statistical Analysis* (second edition). John Wiley & Sons, New York. 675 pp.
- Fleet, D. J. & Jepson, A. D. (1990). Computation of component image velocity from local phase information. *International Journal of Computer Vision*, **5**(1), 77–104.
- Gabor, D. (1946). Theory of communication. *Journal of the Institution of Electrical Engineers*, **93**, 429–457.
- Heeger, D. J. (1987). Optical flow from spatio-temporal filters. In *First International Conference on Computer Vision*, pp. 181–190 London.
- Herlin, I. L., Cohen, I., & Bouzidi, S. (1995). Detection and tracking of vortices on oceanographic images. In *Proceedings of the 9th Scandinavian Conference on Image Analysis*, pp. 689–696 Uppsala, Sweden.
- Horn, B. K. P. & Schunk, B. G. (1981). Determining optical flow. *Artificial Intelligence*, **17**, 185–203.
- Knutsson, H. (1989). Representing local structure using tensors. In Pietikäinen, M. & Rönning, J. (Eds.), *The 6th Scandinavian Conference on Image Analysis*, pp. 244–251 Oulu, Finland. The Pattern Recognition Society of Finland.
- Konrad, J. & Dubois, E. (1992). Bayesian estimation of motion vector fields. *IEEE Transactions on Pattern Analysis and Machine Intelligence*, **14**(9), 910–927.
- Larsen, R., Conradsen, K., & Ersbøll, B. K. (1995). Estimation of dense image flow fields in fluids. , Department of Mathematical Modelling, Technical University of Denmark. 33 pp. (To appear in IEEE Transactions on Geoscience and Remote Sensing.
- Leese, J. A. & Novak, C. A. (1971). An automated technique for obtaining cloud motion from geosynchronous satellite data using cross correlation. *Journal of Applied Meteorology*, **10**, 118–132.
- Nagel, H.-H. & Enkelmann, W. (1986). An investigation of smoothness constraints for the estimation of displacement vector fields from image sequences. *IEEE Transactions on Pattern Analysis and Machine Intelligence*, **8**(5), 565–593.
- Rao, A. R. & Jain, R. C. (1992). Computerized flow field analysis: oriented texture fields. *IEEE Transactions on Pattern Analysis and Machine Intelligence*, **14**, 693–709.
- Schmetz, J. & Holmlund, K. (1993). Operational cloud-motion winds from Meteosat infrared images. *Journal of Applied Meteorology*, **32**, 1206–1225.

ing and the use of regularization. *IEEE Transactions on Geoscience and Remote Sensing*, **42**(3), 479–493.

Terzopoulos, D. (1986). Regularization of inverse visual problems involving discontinuities. *IEEE Transactions on Pattern Analysis and Machine Intelligence*, **8**(4), 413–424.

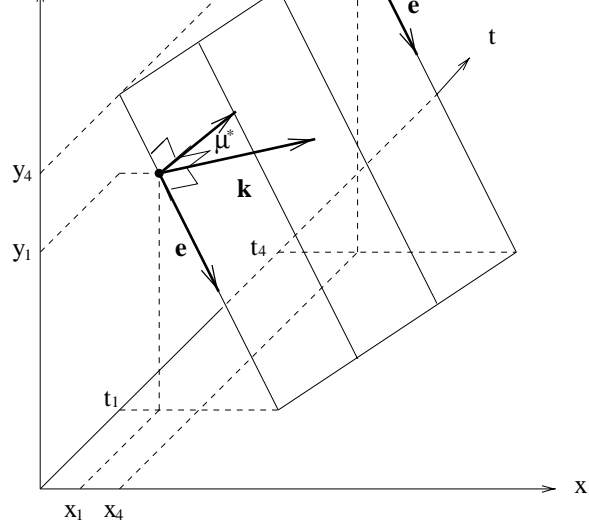


Fig. 1: Relationship between the spatio-temporal orientation vector and the normal flow. The reader is referred to the text for a detailed explanation.

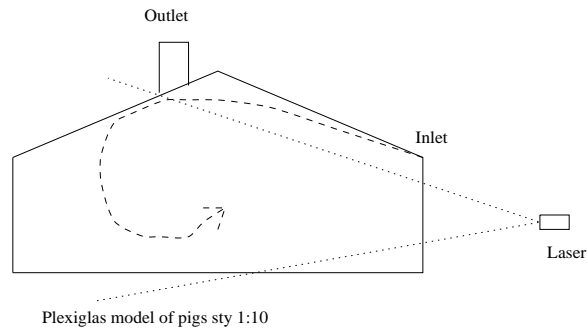


Fig. 2: Experimental setup. The 1:10 Plexiglass model of a segment of a pigs sty is illuminated by a laser sheet. The video camera is placed with its optical axis perpendicular to the laser plane. The air is drawn into the model by putting suction on the outlet.

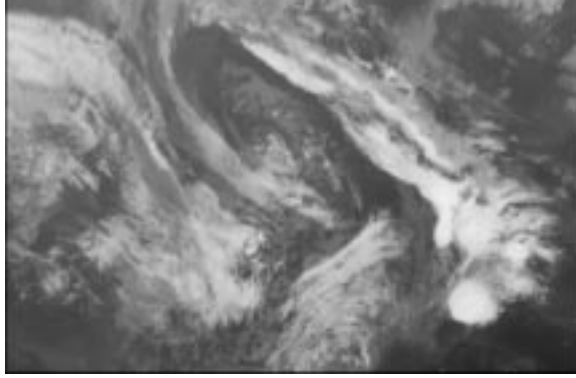


Fig. 3: An image from the Meteosat sequence.

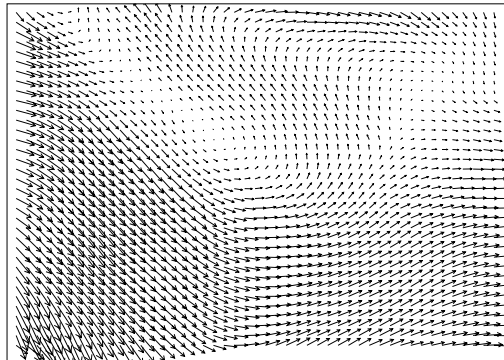


Fig. 4: The flow field corresponding to the cloud image in Figure 3.

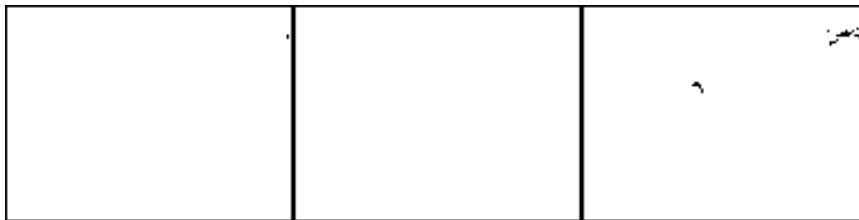


Fig. 5: The three accumulator arrays corresponding to nodes, saddles, and centers/spirals, respectively. By applying a thresholding operation in the likelihood measures we have identified the two centers in the flow field corresponding to the cloud image in Figure 3.

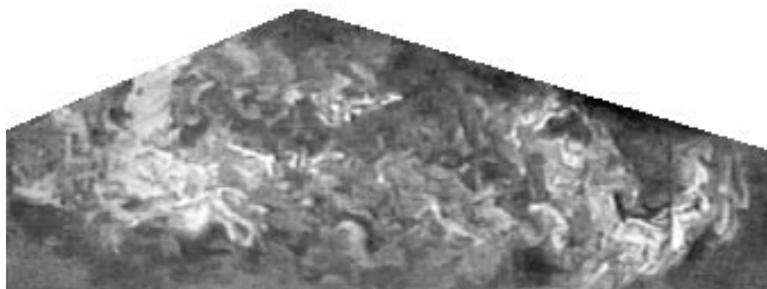


Fig. 6: An image from the livestock airflow sequence.

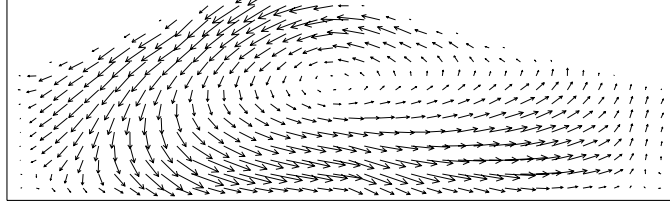


Fig. 7: The flow field corresponding to the livestock airflow image in Figure 6.

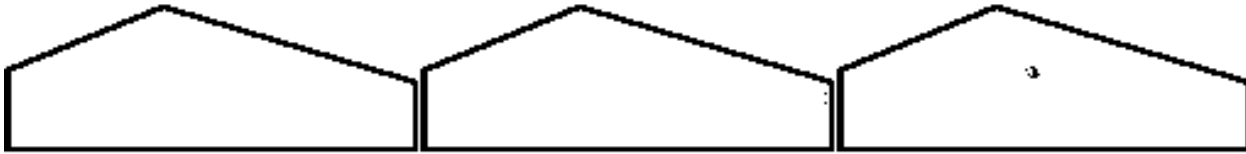


Fig. 8: The three accumulator arrays corresponding to nodes, saddles, and centers/spirals, respectively. By applying a thresholding operation in the likelihood measures we have identified the centers in the flow field corresponding to the livestock building airflow image in Figure 6.

